Distribution of mean kinetic energy around an isolated wind turbine and a characteristic wind turbine of a very large wind farm

Gerard Cortina, Marc Calaf, and Raúl Bayoán Cal

Phys. Rev. Fluids **1**, 074402 — Published 9 November 2016

DOI: 10.1103/PhysRevFluids.1.074402

Distribution of mean kinetic energy around an isolated wind turbine and a characteristic wind turbine of a very large wind farm

Gerard Cortina* and Marc Calaf†
Department of Mechanical Engineering, University of Utah, Utah, USA

Raúl Bayoán Cal‡
Department of Mechanical Engineering, Portland State University, Oregon, USA
(Dated: October 5, 2016)

An isolated wind turbine and a very large wind farm are introduced into Large Eddy Simulations of an atmospheric boundary layer. The atmospheric flow is forced with a constant geostrophic wind and a time varying surface temperature extracted from a selected period of the CASES-99 field experiment. A control volume approach is used to directly compare the transfer of mean kinetic energy around a characteristic wind turbine throughout a diurnal cycle considering both scenarios. For the very large wind farm case, results illustrate that the recovery of mean kinetic energy around a wind turbine is dominated by the vertical flux, regardless of atmospheric stratification. Contrary, for an isolated wind turbine, the recovery is dependent on the background atmospheric stratification and it is produced by a combination of advection, vertical flux and pressure redistribution. The analysis also illustrates that during the unstable stratification periods vertical entrainment of mean kinetic energy dominates, whereas during the stable regime horizontal entrainment is predominant. Finally, it is observed that in both scenarios, the single wind turbine and the large wind farm cases, turbulent mixing is driven by the background convective stratification during the unstable period, and by the effect of the wind turbine during the stable regime.

* gerard.cortina@utah.edu; http://wet.mech.utah.edu
† marc.calaf@utah.edu; http://wet.mech.utah.edu
‡ rcal@pdx.edu

I. INTRODUCTION

Wind energy has stood as a prominent element of the mix of renewable energies, with a remarkable growth of 23% over the past decade [1]. For wind energy to be profitable large arrays of wind turbines, so called wind farms, must be built. However, the capacity for the atmospheric turbulent flow to immediately recover past a succession of wind turbines is limited, inducing power losses and enhanced structural fatigue due to turbine to turbine proximity [2–4]. In a very large wind farm, a fully developed turbulent flow develops, in which the statistical properties of the flow do not change within the horizontal directions, thus relevant changes mostly occur in the vertical direction. Within this region, so called the *wind turbine array boundary layer* (WTABL), the recovery of the successive turbine-generated wakes is only a result of vertical entrainment of mean kinetic energy (MKE) as shown by Lu and Porté-Agel [5], Yang et al. [6], VerHulst and Meneveau [7], Abkar and Porté-Agel [8], which is a function of the wind farm arrangement [9]. This mechanism determines the overall efficiency of the farm as numerically shown in VerHulst and Meneveau [10] for a pressure-driven flow without thermal stratification, in Calaf et al. [11] for a neutrally stratified atmospheric flow and experimentally in Cal et al. [12]. These large wind farms alter the local atmospheric flow with changes in the surface momentum and surface heat fluxes [13], as well as readjusting the Coriolis force balance [14]. Overall, wind farms increase the turbulent mixing with a reduction of momentum entrainment near the surface and a large increase near the top-tip of the rotor blades. These flow alterations change the heat fluxes (sensible and latent) and introduce small perturbations on the surface and air flow temperature [14–17].

A control volume approach to extend the current understanding of the redistribution of MKE and recovery process around a single wind turbine and a characteristic wind turbine of a very large wind farm have been performed during a standard diurnal cycle. Results will illustrate the differences in the redistribution of MKE according to the background atmospheric stratification (stable, unstable and neutral), as well as the relative importance of terms contributing the MKE budget (advection, work produced by the mean pressure field gradient, MKE flux, dissipation, gravitational acceleration of vertical motions and Coriolis forcing).

In section II, the control volume framework used to develop the MKE budget is introduced. Section III presents the study cases considered, and section IV contains the concept of the wind turbine box. Section V presents the results for the aforementioned cases, illustrating the wind turbine box approach. Finally, conclusions are outlined in section VI.

II. CONTROL VOLUME ANALYSIS OF THE MEAN KINETIC ENERGY

The mean kinetic energy equation is obtained by taking the product of the mean velocity, $\overline{U}_i$, and the momentum equation

$$\overline{U}_j \frac{\partial \overline{U}_i}{\partial x_j} = -\frac{1}{\rho}\frac{\partial \overline{P}}{\partial x_i} - \frac{\partial \overline{u_i' u_j'}}{\partial x_j} + \nu \frac{\partial^2 \overline{U}_i}{\partial x_j^2} + \overline{B_i} - \overline{f}_i^{\,\mathrm{wt}} + f_c \epsilon_{ij3} \overline{U}_j, \tag{1}$$

where $(')$ denotes the fluctuations and the overbar $(\overline{\cdot})$ a time averaged quantity. The mean pressure is given by $\overline{P}$, and $\overline{f}_i^{\,\mathrm{wt}}$ represents the force imparted on the flow by the wind turbines. The thermal buoyant forcing is represented by $\overline{B_i} = \beta g (T - T_{ref}) \delta_{i3}$, where β is the coefficient of thermal expansion, g is gravity, T is the mean temperature and T_{ref} is the reference temperature. Respectively, both air flow properties, density (ρ) and kinematic viscosity (ν) are treated as constants. The Coriolis parameter is denoted by f_c, and ϵ_{ij3} is the alternating unit tensor ($\epsilon_{ij3} = 0$, if $i = j$, and ± 1 otherwise). Omission of the time dependence of the velocity field is also noted ($\partial \overline{U}_i / \partial t = 0$). After carrying out the operation, the transport equation for the mean kinetic energy, $K = \frac{1}{2}\overline{U}_i^2 = \frac{1}{2}(\overline{U}^2 + \overline{V}^2 + \overline{W}^2)$, ($\overline{U}$, $\overline{V}$ and $\overline{W}$ being the streamwise, lateral and vertical mean velocities, respectively) is obtained as

$$\begin{aligned} \overline{U}_j \frac{\partial K}{\partial x_j} = &-\frac{\partial}{\partial x_j}\left(\frac{1}{\rho}\overline{P}\,\overline{U}_i \delta_{ij} + \frac{1}{2}\overline{u_i' u_j'}\,\overline{U}_i - 2\nu \overline{S}_{ij}\overline{U}_i\right) \\ &-\overline{u_i' u_j'}\frac{\partial \overline{U}_i}{\partial x_j} - 2\nu \overline{S}_{ij}\overline{S}_{ij} + \overline{U}_i \overline{B} - \overline{U}_i \overline{f}_i^{\,\mathrm{wt}} + f_c \epsilon_{ij3} \overline{U}_i \overline{U}_j, \end{aligned} \tag{2}$$

where $\overline{S}_{ij} = \frac{1}{2}\left(\frac{\partial \overline{U}_i}{\partial x_j} + \frac{\partial \overline{U}_j}{\partial x_i}\right)$ is the mean strain rate tensor. Thereafter and from left to right, the terms in (2) are the advection of mean kinetic energy, mechanical work produced by gradients in the mean pressure field, two flux terms: mean kinetic energy by turbulence and viscous dissipation, production of turbulence kinetic energy, mean viscous

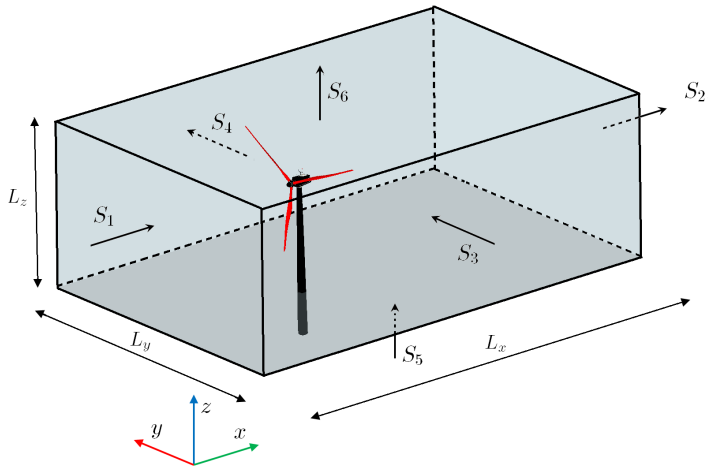

FIG. 1. Rectangular control volume (CV) around the wind turbine used for an extended momentum analysis. The coordinate system denoted by x, y, z is the referent axis for the CV. The size of the CV is denoted by L_x, L_y and L_z which represent the streamwise, spanwise and vertical dimensions respectively. The CV surfaces are denoted by S_i, where i indicates any of the CV surfaces (from 1 to 6).

dissipation, mean kinetic energy production or destruction by buoyancy forces, power extracted by the wind turbine and finally the last term denotes the effect due to Coriolis force.

In marking a control volume (CV) around a turbine, a volume integral of the transport Equation (2) is taken as shown in Figure 1. In the CV of Figure 1, the surfaces normal to the longitudinal direction, acting as inflow and outflow are denoted S_1 and S_2, lateral surfaces as S_3 and S_4, and horizontal bottom and top surfaces as S_5 and S_6. Hence, the volume integral of Equation (2) reads as

$$\overbrace{\iiint_V \overline{U}_j \frac{\partial K}{\partial x_j} dV}^{A_1} = -\overbrace{\iiint_V \frac{\partial}{\partial x_j}\left(\frac{1}{\rho}\overline{P}\,\overline{U}_i\delta_{ij} + \frac{1}{2}\overline{u_i' u_j'}\,\overline{U}_i - 2\nu\overline{S}_{ij}\overline{U}_i\right) dV}^{A_2}$$
$$- \underbrace{\iiint_V \overline{u_i' u_j'}\frac{\partial \overline{U}_i}{\partial x_j} dV}_{A_3} - \underbrace{\iiint_V 2\nu\overline{S}_{ij}\overline{S}_{ij} dV}_{A_4} + \underbrace{\iiint_V \overline{U}_i \overline{B} dV}_{A_5}$$
$$- \underbrace{\iiint_V \overline{U}_i\,\overline{f}_i^{\,\mathrm{wt}} dV}_{A_6} + \underbrace{\iiint_V f_c \epsilon_{ij3}\overline{U}_i\overline{U}_j dV}_{A_7}, \tag{3}$$

where the triple integral notation stresses that dV is a closed volume.

To simplify the discussion, terms are labeled as A_n, where n runs from one to seven as shown in the over/underbrackets in Equation 3. Sequentially, these constitute the inertial terms (A_1), the transport/flux terms denoted by A_2, production of turbulence kinetic energy (A_3) and A_4 contains the mean viscous dissipation. Finally, three body force terms encompassing the buoyancy, the power extracted by the turbine and the Coriolis effect, respectively as A_5, A_6 and A_7, are also represented by the previous Equation 3. Introducing the divergence theorem, the volume integral of the advection of mean kinetic energy on the left hand side is rewritten as a surface integral

$$A_1 = \iint_S (\overline{U}_i K)\hat{n}_i \, dS, \tag{4}$$

where $\hat{n}_i$ is the unit vector normal to the surface S of the CV. A similar treatment is applied to the volume integral of the transport terms of mean kinetic energy on the right hand side

$$A_2 = \iint_S \left(\frac{1}{\rho}\overline{P}\,\overline{U}_i\delta_{ij} + \frac{1}{2}\overline{u_i' u_j'}\overline{U}_i - 2\nu\overline{S}_{ij}\overline{U}_i\right)\hat{n}_j \, dS. \tag{5}$$

TABLE I. Study cases for the LES numerical simulations

Study case	VLWF	VLWF	VLWF	LSWF	LSWF	LSWF
ABL stratification	Unstable	Neutral	Stable	Unstable	Neutral	Stable
# of Turbines	48	48	48	1	1	1
$s_x \times s_y \approx$	$8D \times 5D$	$8D \times 5D$	$8D \times 5D$	$63D \times 31D$	$63D \times 31D$	$63D \times 31D$

Because the components of velocity tangent to the surface do not contribute to the flux across the control surface, since in such a case $\vec{u} \cdot \vec{n} = 0$, the surface integral of mean kinetic energy advection simplifies to

$$A_1 = -\iint_{S_1} \overline{U} K dS_1 + \iint_{S_2} \overline{U} K dS_2 - \iint_{S_3} \overline{V} K dS_3 + \iint_{S_4} \overline{V} K dS_4 - \iint_{S_5} \overline{W} K dS_5 + \iint_{S_6} \overline{W} K dS_6, \tag{6}$$

and surfaces are visualized in Figure 1. Moreover, evaluating the various components within terms A_3 through A_7, the volume integral is considered. In expanding term A_3, for example, the volume is composed of the differentials in the three directions, x, y and z, and the corresponding stress term results

$$A_3 = \iiint_V \left(\overline{u'u'} \frac{\partial \overline{U}}{\partial x} + \overline{u'v'} \frac{\partial \overline{U}}{\partial y} + \overline{u'w'} \frac{\partial \overline{U}}{\partial z} + \overline{v'u'} \frac{\partial \overline{V}}{\partial x} + \overline{v'v'} \frac{\partial \overline{V}}{\partial y} + \overline{v'w'} \frac{\partial \overline{V}}{\partial z} + \overline{w'u'} \frac{\partial \overline{W}}{\partial x} + \overline{w'v'} \frac{\partial \overline{W}}{\partial y} + \overline{w'w'} \frac{\partial \overline{W}}{\partial z} \right) dx\, dy\, dz. \tag{7}$$

Therefore, it is understood that similarly it is obtained for the viscous dissipation, buoyancy, power extracted by the wind turbines and the Coriolis terms in Equation 3. Note that terms developed here correspond to the most general form of the MKE budget in a CV. These are correspondingly adapted to match the large eddy simulations (see section V A), which consist of a resolved and a subgrid stress contribution and neglect the viscous effects as a result of the high Reynolds number characteristic of atmospheric flows.

III. STUDY CASES

To develop this study, a suite of six LES cases are performed: three with a very large wind farm (VLWF), and three with a single wind turbine or largely spaced wind farm (LSWF). Table I summarizes the study cases. For both, the LSWF and VLWF, a simulation consisting of a complete diurnal cycle (total of 24hours in physical time) is developed obtaining consecutive periods with stable (night-time) and unstable (day-time) atmospheric stratification. The diurnal cycle is forced using a height-independent and time-constant geostrophic wind together with a time-varying surface temperature. The geostrophic wind $(\mathrm{u_G}, \mathrm{v_G}) = (9, -3)\mathrm{ms}^{-1}$, and the surface temperature (see Figure 2a) are extracted from the CASES-99 (Cooperative Atmosphere-Surface Exchange Study - 1999) [18] field experiment between October 22-24 of 1999 and validated using results from Kumar et al. [19, 20], Svensson et al. [21] and Basu et al. [22], as well as experimental data from the CASES-99 data-set. Details on the LES framework can be found in previous works by Sharma et al. [23] and Cortina et al. [24]. The time period used to force the diurnal cycle has been previously used in studies of wind farms within a realistic atmospheric boundary layer diurnal cycle by Fitch et al. [25] and Sharma et al. [23] and adopted here as well. Additionally, two independent cases forced with the same geostrophic forcing but with a fixed surface temperature and a well-mixed temperature profile are considered to simulate the case of a neutrally stratified ABL flow.

The time evolution of the surface temperature used to force the flow through a diurnal cycle is represented in Figure 2a, and the corresponding surface stability parameter (z_1/L) is shown in Figure 2b, where $z_1 = \Delta_z/2$ and Δ_z represents the vertical grid spacing. While the atmospheric flow through a diurnal cycle is intrinsically non-stationary, mean statistics over one-hour periods remain fairly unchanged. Here, results for the one-hour periods between 0400 and 0500h (p1) and between 1500 and 1600h (p2), are presented representative of a stable and unstable atmospheric stratification, respectively. The same analysis is applied on other one-hour time periods through the different stable

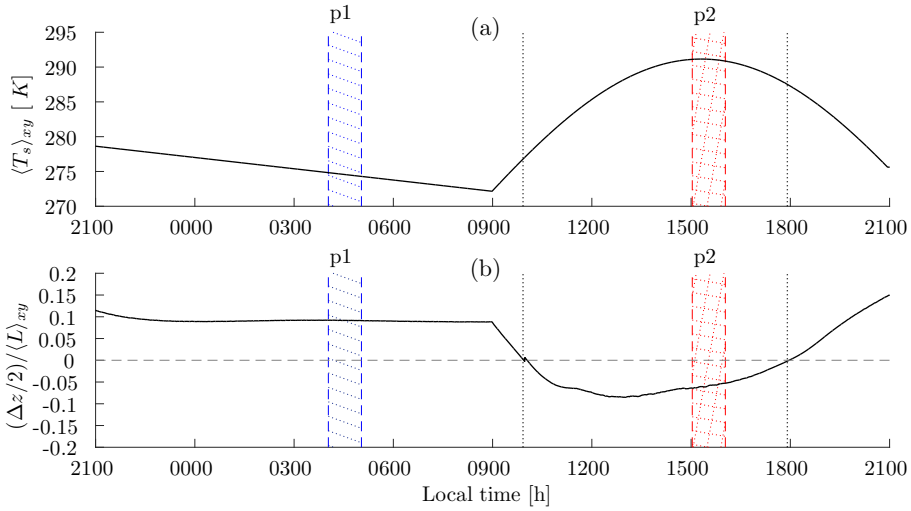

FIG. 2. (a) Horizontally averaged and time-dependent imposed temperature at the surface of the domain $\langle T_s \rangle_{xy}$ $[K]$; (b) normalized stability parameter, $(\Delta z/2)/\langle L \rangle_{xy}$, where $(\Delta z/2)$ is the height of the first grid-point and L is the Monin-Obukhov length as a function of time. One-hour periods marked with 45 degree dotted line (p1), in blue, and squared dotted line (p2), in red, delineate time periods in which mean kinetic energy budgets and representative statistics are computed. Precisely, period p1 constitutes the time between 0400 and 0500h local time (LT) and p2 denotes the time between 1500 and 1600h of LT.

and unstable regimes, obtaining similar convergence in the statistics. A similar one-hour period is also analyzed for the neutrally stratified flow. For both cases, the LSWF and VLWF, the numerical domain is set to $(2\pi \times \pi \times 3)z_i$, where z_i is the initial height of the boundary layer, with $z_i = 1000m$. In order to keep a high numerical resolution, the computational domain is discretized with a numerical grid of $256 \times 128 \times 384$ points, providing a uniform grid resolution of $\Delta_x = \Delta_y = 24.5m$ and $\Delta_z = 7.8m$. The simulations are initialized with the velocity and temperature vertical profiles extracted from the CASES-99 field experiment; corresponding to a height-independent geostrophic wind and a well-mixed temperature profile matching the initial surface temperature of $278.6K$, with an inversion layer spanning from z_i to the top of the domain $(3z_i)$.

The VLWF configuration consists of eight rows with six wind turbines per row, using the traditional spacing of $\sim 8D$ and $\sim 5D$ (where D refers to the rotor diameter of the turbine, here taken equal to $100m$) in the streamwise and spanwise directions, respectively as observed in Figure 3a. Because of the periodic boundary conditions, this configuration results in practical sense equivalent to an infinite wind farm. On the other hand, the LSWF configuration, represented in Figure 3b, consists of a single wind turbine installed in the middle of the domain, and hence it is understood as a single isolated wind turbine, or as a result of the periodic boundary conditions, as a largely spaced wind farm, with a wind turbine spacing of $\sim 63D$ and $\sim 31D$ in the streamwise and spanwise directions, respectively. In both configurations, the algorithm of Sharma *et al.* [26] is used to model the wind turbines, using an upstream scanning distance of $D/2$ to learn from the incoming wind vector and timely readjust the yaw angle of the turbines every ten minutes, cf. Cortina et al. [24].

Differences in transport and recovery of MKE around an isolated wind turbine and a characteristic wind turbine within a wind farm are evaluated herein. To demonstrate the selected study periods, Figure 4 presents the time evolution of ten-minute averaged and horizontally averaged (between the top tip and bottom tip of the rotor) MKE for both cases, the VLWF (dash) and the LSWF (solid) throughout the diurnal cycle. First, it should be noted that while the LES numerical simulation is exactly the same for both wind farms scenarios, a large difference in MKE is observed between them. During the stable stratified period (i.e. from 0000 to 0900h), there exists ~ 4 times more energy in the LSWF than in the VLWF case. This is the result of the increased MKE absorption of the large wind farm. Further, the stable-LSWF period is characterized by a nocturnal low level jet (LLJ) intersecting the wind turbines rotor and hence accounted in this MKE representation, while for the VLWF case the low level jet is shifted above the wind turbines hub layer (see Lu and Porté-Agel [14], Sharma et al. [23], Fitch et al. [25] and Abkar et al. [27]). This effect results in large energy differences between both stable conditions. On the other hand, the unstable periods are dominated by enhanced atmospheric mixing and hence the difference in available energy between the LSWF and the VLWF case is reduced. The unstable-LSWF regime (i.e. from 1300 to 1800h) in average has 1.5 times more energy than the unstable-VLWF case. These differences in available energy will be further illustrated later within the analysis of MKE redistribution. Also, it should be noticed the trend of MKE as a function of time. While for the LSWF more energy is available during the stable period ($\overline{MKE}_{unstable} = 1.2\overline{MKE}_{stable}$), for the VLWF

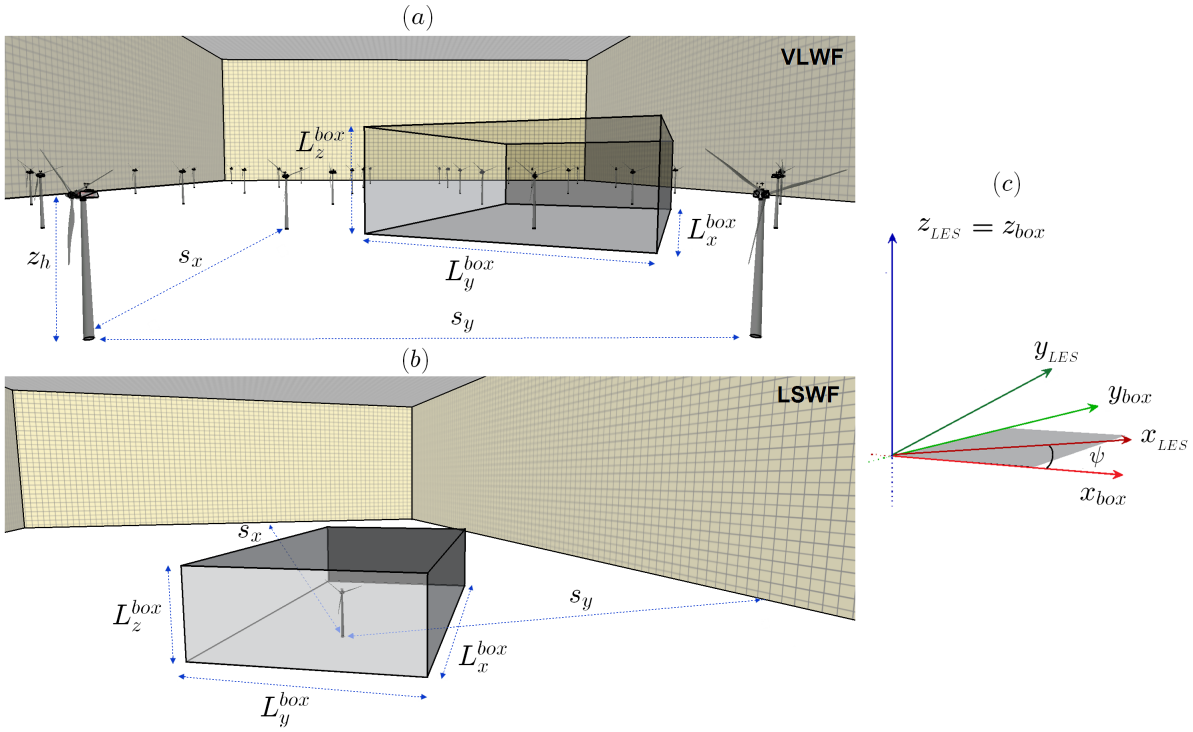

FIG. 3. (a) Very large wind farm case (VLWF); (b) Largely spaced wind farm case (LSWF); (c) Graphical representation of the rotation between the LES domain coordinate frame and the wind turbine box.

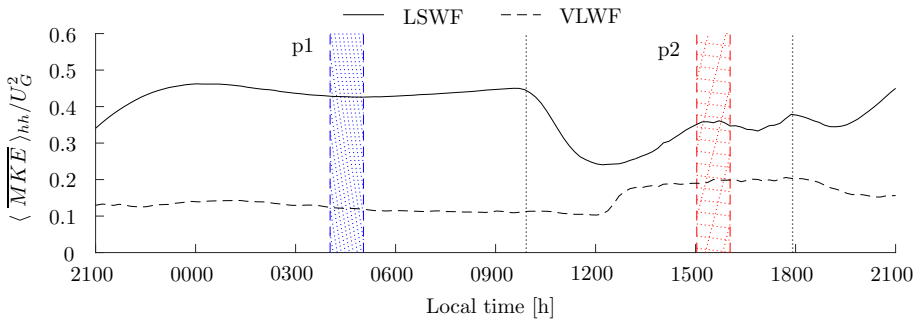

FIG. 4. Mean kinetic energy represented every 10 minutes and averaged over the volume capturing the wind turbine rotor disk (from $z_h - D/2$ to $z_h + D/2$, where $z_h = 100$ m is the hub height and D is the wind turbine diameter) normalized by the square of the geostrophic wind (U_G). The MKE is represented for the LSWF and VLWF cases during the diurnal cycle. Correspondingly, the 45 degree dotted line region (p1), in blue, and the squared dotted region (p2), in red, identify the one-hour stable and unstable stratification periods.

it results the opposite; being the unstable or convective regime the one that presents the largest MKE available ($\overline{MKE}_{unstable} = 0.5\overline{MKE}_{stable}$). Further, it is worth noting that the MKE for the VLWF case presents a change of 30% within hours 1200 to 1400h and then reaching a quasi-stationary state. And for the LSWF, there is an apparent constant change in the MKE ($\sim 5\%/h$) from 1200 to 1500h.

IV. THE WIND TURBINE BOX

To directly compare the flow around a single wind turbine and the flow around a wind turbine installed within a very large wind farm, a dynamically time-realigned CV surrounding each wind turbine, from here on referred as wind turbine box, is developed. The wind turbine box consists of a reduced domain of adjustable size, with the box-local streamwise direction timely aligned perpendicular to the actual rotor disk (see Figure 5a-d). Within this

work, the box of the turbine is selected with a dimension of $(L_x^{box}, L_y^{box}, L_z^{box}) = (9D, 5D, 7D/4)$, and centered around the rotor. Precisely, the box extends between a distance of $2D$-upstream and $7D$-downstream of the disk in the streamwise direction, and $2.5D$ left and right of the hub of the rotor in the cross-streamwise direction, respectively. In the vertical direction, the box is selected to extend a vertical distance between $z_h - 3D/4$ and $z_h + D$. The box size has been selected of equal size for both study cases (the VLWF and LSWF) to be able to compare statistics. Therefore given the limited spacing in the VLWF case, the box is selected to capture the maximum wake region without including the effect of the following wind turbine. It is then possible to evaluate terms as developed in section II from the standpoint of the wind turbine box as the CV goes hand in hand with the analysis.

The wind turbine box is designed such that its corresponding streamwise axis (x_{box}) is timely perpendicular to the rotor disk, and hence aligned with the mean wind vector. The flow variables are initially computed within the base LES coordinate frame (x_{LES}, y_{LES}, z_{LES}) and then transformed into the new box coordinate frame (x_{box}, y_{box}, z_{box}). The mapping transformation consists of a rotation around the vertical axis ($z_{LES} = z_{box}$), which remains frame invariant and it is represented by a rotation matrix, denoted by $\mathbf{R}$ with a rotation angle denoted by ψ, which represents the horizontal angle between the LES domain and box coordinate system (see Figure 3c). Note that through the resultant coordinate transformation, the LES mean flow direction becomes the box local streamwise direction ($\vec{u}_{box} = \mathbf{R}\,\vec{u}_{LES}$). Similarly, the Reynolds stress tensor components are transformed using the corresponding matrix transformation $\tau_{\text{box}} = \mathbf{R}\,\tau_{\text{LES}}\,\mathbf{R^T}$, where $\mathbf{R^T}$ indicates the transpose of the rotation matrix. Figure 3a and 3b illustrates the structure of the wind turbine box within the LES domain for the VLWF and LSWF cases respectively, and the schematics of the frame rotation $(x_{LES}, y_{LES}, z_{LES}) \rightarrow (x_{box}, y_{box}, z_{box})$ is represented in Figure 3c.

V. RESULTS

A. Flow around a characteristic wind turbine

In Figure 5, subplots a-d represent one-hour averaged velocity field for both cases, the VLWF and LSWF, and for both stratification periods (stable and unstable) at hub height. In Figure 5a, the unstable regime causes the turbine wakes to be shorter and less organized due to the increased mixing characteristic of unstable regimes; this is especially the case in the VLWF. In contrast, wakes visibly persist over longer distances and overall are more organized during the stable regime (see Figure 5b), as a result of the attenuated mixing due to turbulence. While the flow for the neutral stratification is not represented here, the flow shows a similar signature as that in the unstable regime, where the turbine wakes expansion results in a radial shape; symmetrically in both directions (x-y plane), also reported by Abkar and Porté-Agel [9]. Rather than considering a wind farm, Figures 5c and 5d highlight a single turbine under unstable and stable regimes, respectively. Wake features are similar to those in the wind farm although these are exaggerated due to the lack of turbine-turbine wake interaction. In these cases, the difference between the expansion of the wake is shaped in the length of itself. Subplots 5c and 5d illustrate that the length of the wake during the stable regime is twice as large as for the unstable period. Also, it should be noted that the yaw alignment has an effect in the wake length and persistence. During the one-hour stable period (p1) the standard deviation of the wind angle is $\sim 1°$, while for the unstable period the standard deviation is $\sim 5°$ (cf. Cortina et al. [24]). This results in a more dynamic wind turbine force acting into the flow in time and space during the unstable regime.

Using the CV approach previously described, a comparison between the flow around a single wind turbine (LSWF) and a characteristic wind turbine within a very large wind farm (VLWF) is sought out. This last one is obtained by averaging the flow of the 48-turbine boxes (one per wind turbine of the LES domain). Figure 5e-h presents one-hour averaged streamwise velocity field at hub-height (using the wind turbine box) for the unstable (left column) and stable (right column) regimes. From this representation, the flow around both wind turbine scenarios (VLWF represented in e-f and LSWF represented in g-h) is very distinct between atmospheric stability conditions. From Subplots 5e-h, it can be observed that both types of turbines present different wake geometry. Flow features show changes in both streamwise and cross-streamwise directions. Figure 5e is the characteristic unstable wake, having a practically symmetric expansion in the horizontal direction. Instead, Figure 5f shows a slimmer and sharper shape with an irregular expansion, characteristic of the stable wake. Also, this last one shows a velocity deficit upstream of the wind turbine, signature of the turbine-wake interaction. Even though Figure 5e should be showing a velocity deficit upstream of the wind turbine rotor, this is much more attenuated and practically nonexistent, due to the convective regime present during the unstable stratification. For the LSWF, no upstream velocity deficit due to the fact that in these cases there are no upstream turbines. Also, it should be noted that for the stable-VLWF case Figure 5f, as a result of the overall wind reduction, the wake deficit is attenuated in comparison to the stable-LSWF case 5h. In general, a more rapid wake recovery is observed for the unstable-VLWF case, with the wake recovering to 90% of the inflow wind speed at $5D$ and $6D$ downstream from the rotor disk for the unstable-VLWF and unstable-LSWF cases, correspondingly.

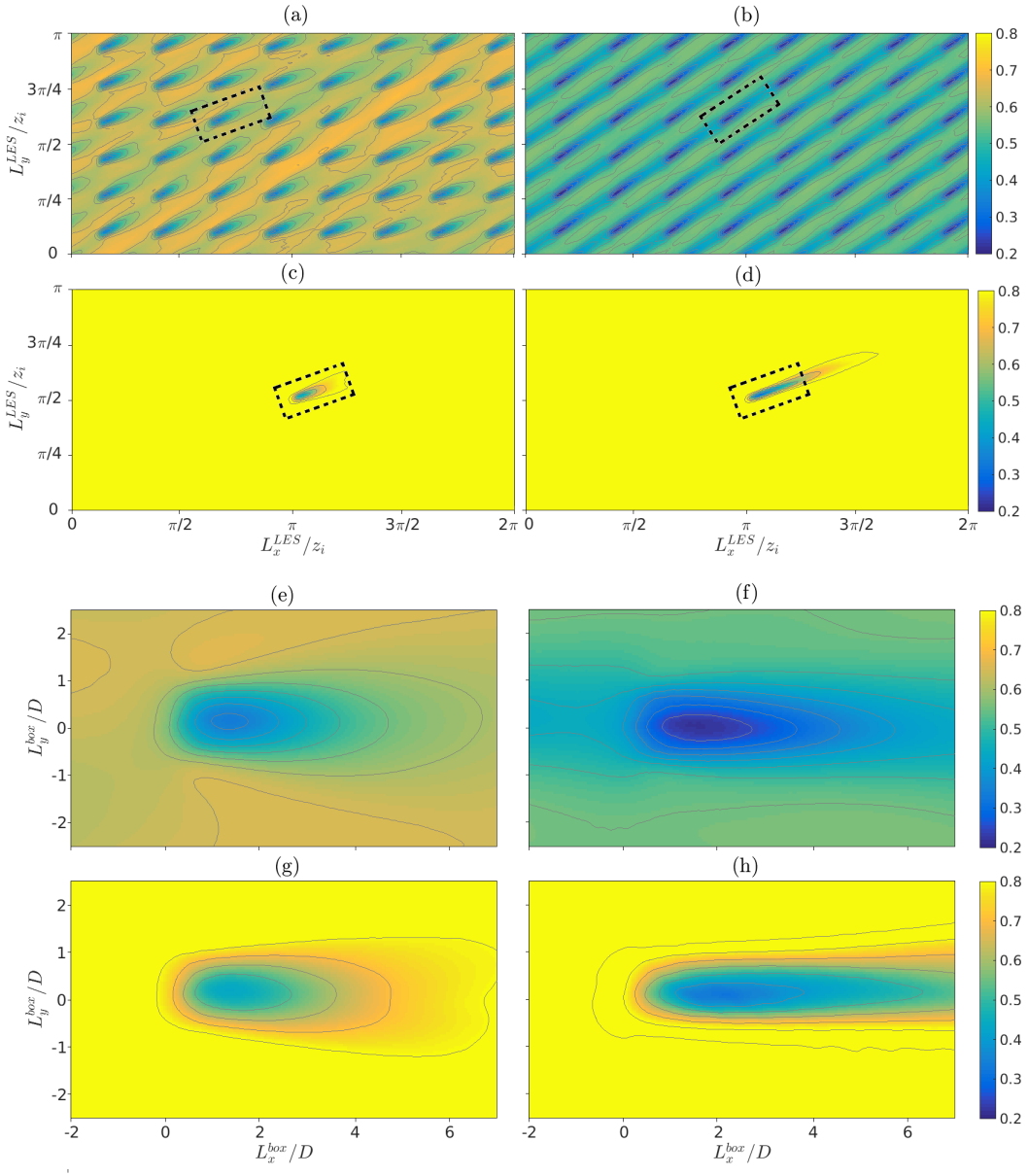

FIG. 5. Sub-figures a-d depict the LES domain horizontal slices of one-hour averaged, normalized velocity magnitude fields at hub height for two characteristic periods of the VLWF and LSWF simulations. (a) unstable-VLWF, (b) stable-VLWF, (c) unstable-LSWF, (d) stable-LSWF. And sub-figures e-f depict the horizontal slices of one-hour averaged, normalized velocity magnitude at hub height within the wind turbine box reference frame. (e) unstable-VLWF, (f) stable-VLWF, (g) unstable-LSWF, (h) stable-LSWF. The dashed line surrounding the wind turbine in Sub-figures a-d represents the wind turbine box.

B. Mean kinetic energy fluxes around a characteristic wind turbine

The MKE terms previously described in Section II are now redefined within the LES framework, and the nomenclature denoted in Expression 8 will be used from now on.

$$0 = A + P + \phi + \epsilon + G_a + P_{WT} + C_g. \tag{8}$$

In the above expression, A represents the advection term, denoted as A_1 in Equation 3. The work due to pressure gradients on the mean flow is denoted by P and ϕ denotes the turbulent flux of MKE, these two terms correspond to the first and second terms denoted as A_2 in Equation 3. The dissipation term denoted as ϵ in Expression 8 corresponds

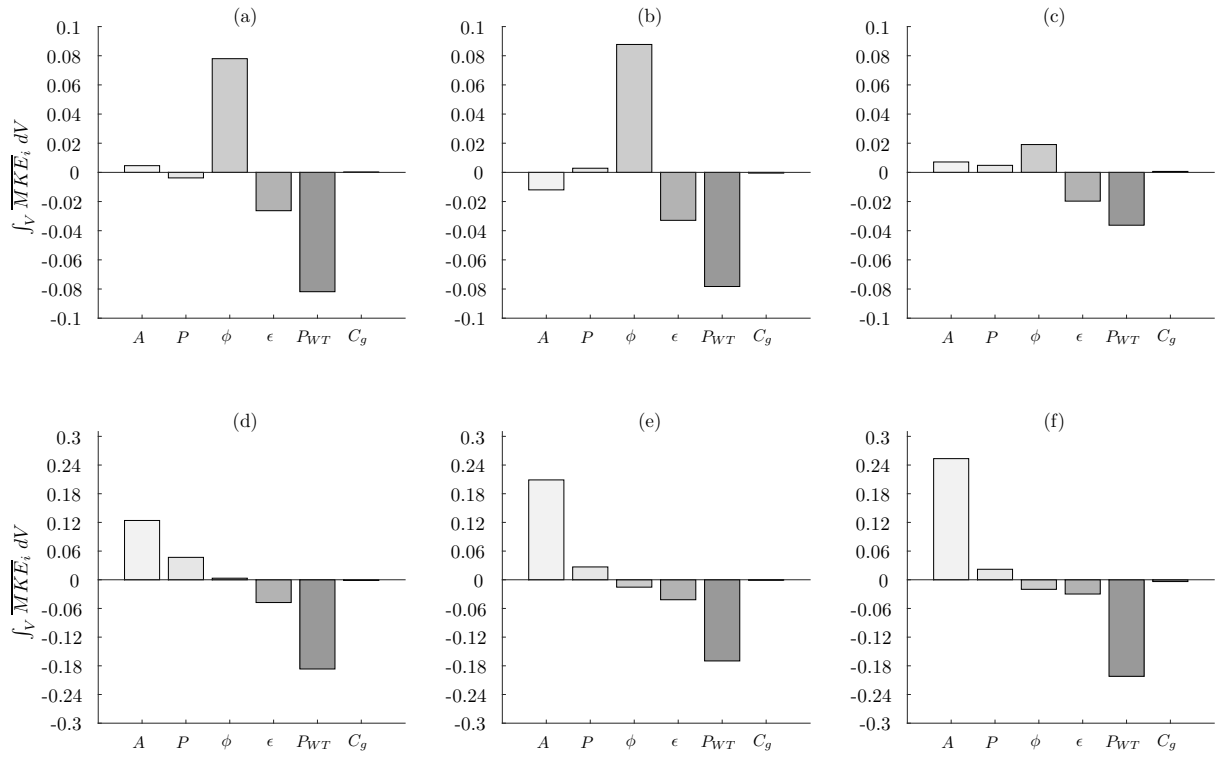

FIG. 6. Bar representation of the volume integral for the different MKE terms (MKE_i) within the wind turbine box. The sub-index i represents the different terms contributing to the MKE budget (Equation 8) where A, P, ϕ, ϵ, P_{WT}, and C_g, represent the advection, work due to pressure gradients on the mean flow, turbulent flux of MKE, dissipation, wind turbine power extraction and the Coriolis effect, respectively. Subplots (a), (b) and (c) depict the VLWF case for unstable, neutral and stable stratifications. Subplots (d), (e) and (f) depict the LSWF case for the unstable, neutral and stable stratifications, correspondingly.

to term A_3, and the gravitational acceleration of vertical motions is represented by G_a, which corresponds to term A_5. Note that the difference between terms A_5 and G_a (see Equation 9) is due to the use of the Boussinesq approximation within the LES framework. The wind turbine power extraction is identified by P_{WT} and corresponds to term A_6, and finally C_g denotes the effect of the Coriolis forcing, which corresponds to term A_7 in Equation 3. Notice that the third term from A_2, and term A_6 are representative of the viscous effects, which are being neglected, as it is traditional in LES of atmospheric flows because the atmospheric flow is characterized by very large Reynolds number. Therefore, following Equation 2 and 3 from Section II, the corresponding terms of the MKE budget using the LES framework are represented by

$$A = -\overline{U}_j \frac{\partial K}{\partial x_j}, \quad P = -\frac{\overline{U}_i}{\rho}\frac{\partial \overline{P}}{\partial x_i}, \quad \phi = -\frac{\partial(\overline{\tau}_{ij}\overline{U}_i)}{\partial x_j}, \quad \epsilon = \overline{\tau}_{ij}\frac{\partial \overline{U}_i}{\partial x_j},$$
$$G_a = -g\left(\frac{\overline{U}_i\overline{\theta}}{\theta_{ref}}\right)\delta_{i3}, \quad P_{WT} = \overline{U}_i\overline{f}_i^{\,\mathrm{wt}}, \quad C_g = f_c\epsilon_{ij3}\overline{U_iU_j}, \tag{9}$$

where $\overline{\tau}_{ij} = \overline{u_i'u_j'} + \overline{\tau}_{ij}^{SGS}$ is the sum of the Reynolds and the sub-grid scale (SGS) shear stress.

Figure 6 illustrates the integral for the previously described MKE terms within the CV. This figure best illustrates the differentiated behavior in the wake recovery between the VLWF and the LSWF. For the VLWF (6a-c), the power harvested by the turbines corresponds to the remaining balance between the MKE dissipation and the turbulent flux of MKE; the contribution of the flux of MKE into the power harvested represents a 72%, 79% and 34% for the unstable, neutral and stable, respectively. Then, it is concluded that in this case, the transport term is the main responsible for the recovery of MKE within the turbine region, where the advection and pressure redistribution terms only provide a marginal contribution to the budget balance. Contrary, for the LSWF (6d-f) the harvested power is recovered mainly through the advection term (being 83%, 98% and 109% with respect to the sum of the harvested power and dissipation for the unstable, neutral and stable regimes, respectively) and the pressure redistribution (being

20%, 13% and 9% with respect to the sum of the harvested power and dissipation for the unstable, neutral and stable regimes, respectively). Note that for the LSWF scenarios the budget has a residual of 3%, 11%, and 18% for the unstable, neutral and stable regimes, respectively. Also, it is relevant to note a factor of two between the advection term for the unstable (6d) and stable (6f) stratification cases for the LSWF cases.

This section should be concluded by stating that for the VLWF scenarios, independently of the flow stratification, the MKE is transported mainly by turbulent flux, decreased by viscous dissipation and power extracted by the wind turbine. Instead, the LSWF case is highly dependent in the stratification and differences are observed among them. While the MKE is always decreased by viscous dissipation and power extraction for the three studied stability conditions; emphasis should be placed in how the MKE is recovered or transported. While for the unstable stratification the MKE is mainly recovered within the CV by advection, pressure and a very small contribution of turbulent flux of MKE, in the stable case the balance is practically due to advection with a very small contribution of the pressure term, with the the turbulent flux having a negative contribution, also depicted in the neutral-LSWF case. Besides, the neutral case is a scenario that fits in between the unstable and stable cases.

To observe further details of the flow around an isolated wind turbine and the flow around a turbine within a large wind farm, the terms contributing to the budget of the MKE are now represented using a spatially distributed wind turbine box analysis, as presented in Section II. For example, Figure 7 illustrates the contribution of the surface terms of MKE (A, ϕ and P) through the control surface delimiting the wind turbine box, as well as horizontal slices at different heights ($z_h - D/2$, z_h and $z_h + D/2$), of the volumetric terms contributing to the MKE budget (P_{WT}, ϵ and C_g). The case represented in Figure 7 corresponds to the LSWF case during the unstable regime. Influx terms to the CV are considered positive, while the outflux terms are considered negative. Each ones of the top six subplots represents a different side of the wind turbine box (front (S_1) and back (S_2) lids, right (S_3) and left (S_4) lids and bottom (S_5) and top (S_6) lids). The subplot located at the center represents the right plane (S_3) of the box and the upper and lower one represent the top (S_6) and bottom (S_5) lids, correspondingly. Note that these lids have the vertical axis inverted, so they perfectly connect with the right-side plane. Next, the centered left and centered right subplots represent the front (S_1) and back (S_2) faces of the wind turbine box. Finally the isolated, top-left subplot represents the left plane of the box (S_4). Within the front side, the geometry of the rotor disk is delineated with a dashed black line for the sake of reference. Note that the front plane (S_1) is taken 2D upstream of the rotor disk.

Of special interest is the top lid subplot (S_6), where it can be observed an outflow of MKE from 2D upstream of the rotor disk to the rotor disk plane. Right behind the rotor disk, an entrainment region is observed for about 2D, and then an outflow of MKE is measured, linked to the wake growth. An inverted behavior between the left and right sides of the wind turbine box is also present as a result of the rotation of the wake. There exists an influx at the top half of the right side of the surface S_3 with an outflux on the lower side. The opposite trend is shown in the left side, surface S_4. Finally, there is only an outflux of MKE through the back of the wind turbine box (S_2). It is interesting to note that the outflux pattern is directly related to the wake of the turbine, which is vertically slanted.

To complete the picture, the spatial contribution of the MKE volumetric terms are also considered and represented through the lower 9 subplots in Figure 7. These terms illustrate the contribution to the MKE of the Coriolis forcing (first column), the dissipation of MKE (second column), and the power extracted by the turbines from the atmospheric flow (third column). Within each column, the different rows illustrate slices of the volume terms at different heights. From top to bottom these correspond to $z_h + D/2$, z_h, and $z_h - D/2$. In all subplots, the contribution of the turbine wake and turbine rotor are quite apparent. In C_g, the turbine influences the term as two dipole features appear immediately at the rotor disk and these depend on the vertical location z; being most marked at mid span $z = z_h$. The signature in the wake is contrary to that at the rotor but with lessened magnitudes. When considering the dissipation term (ϵ), once again as a function of height, it shows the signature of the rotor disk, strongly marking the lateral wind turbine effects at hub height, and intensively noticeable at the center location of the wind turbine for the top and bottom subplots. Finally, a significant sink is present at the exact location of the disk corresponding to the term P_{WT}. The diffuse effect of the rotor disk is due to the continuous realignment of the rotor throughout the one-hour averaging period.

In considering all cases, Figure 8 represents streamwise profiles of the CV vertically integrated flux terms, through the lateral surfaces (S_3 and S_4). Also, streamwise profiles of horizontally integrated flux terms through the bottom and top surfaces (S_5 and S_6) are denoted. While the wake recovery process is fully captured with this wind turbine box size for the VLWF case, for the LSWF case it is not, given the large extent of the wake. However, the same turbine box is used for like-to-like comparisons. Asymmetry is present in the lateral fluxes of MKE for all studied cases, meaning that the MKE entering through one side, S_4, leaves almost entirely through the other side, S_3, throughout the entire length of the CV. With opposite behavior, the flux of MKE through the top lid is highly dependent on the case, thus reflecting the influence of atmospheric stratification and number of turbines. For the VLWF case during the unstable regime (see Figure 8a), an asymmetry exists in the MKE fluxes through the top and bottom lids. Clearly, a net influx (58% with respect to the total influx at 4D downstream of the wind turbine rotor) of MKE penetrates through the top lid, and the flux through S_4 results of the same order of magnitude. A similar trend for the influx

through the top lid S_6 is present during the VLWF neutral stratification, resulting in an influx of 84% with respect to the total influx at 4D downstream of the wind turbine rotor (see Figure 8b). Here a reduction of the horizontal flux is denoted, being this close to 6 times smaller than the flux through S_6. Interestingly, the stable-VLWF shows a practically null vertical entrainment from the wind turbine rotor to 6D downstream, where the vertical MKE flux through the top lid (S_6) starts to show up. This case, is mainly driven by horizontal MKE flux through lid S_4. For the distinct LSWF scenarios, vertical entrainment of MKE is barely visible, except for the unstable case, where the flux through the top lid becomes important from 2D downstream of the rotor disk. It is interesting to denote that for the stable-LSWF, the horizontal flux of mean kinetic energy is remarkable, occurring along the entire length of the wind turbine box. Also it should be noticed that this case and the neutral-LSWF case are the only ones that present a negative flux through S_6 after the wind turbine rotor. This means that there exists an outflux of MKE, results of the vertical expansion of the wake.

By integrating the MKE fluxes through the corresponding CV faces, it is possible to better quantify the relevance of the vertical entrainment of MKE in the recovery process of the depletion of MKE induced by the presence of the turbines. This is illustrated in Figure 9 by means of a bar representation. Each bar, indicates the corresponding contribution of MKE through each face of the wind turbine box (S_1, S_2, S_3, S_4, S_5, S_6) and V representing the sum of the volume terms. As it could be expected, the major inflow and outflow of MKE occurs through the front (S_1) and back (S_2) faces of the wind turbine box. Note that the represented terms through faces S_1 and S_2 are divided by a factor of 2 for the VLWF and a factor of 4 for the LSWF case; for the sake of better inter-comparison of these terms. Furthermore, in the VLWF case these contributions are almost perfectly asymmetrical (influx, S_1, versus outflux, S_2) totaling to 0.48 and -0.46 for the unstable stratification (9a), 0.62 and -0.62 for the neutral (9b) and 0.58 and -0.58 for the stable one (9c). Interestingly, this behavior is not as clear for the LSWF, where the values are 1.28 and -1.08 for the unstable stratification (9d), 1.72 and -1.44 for the neutral (9e) and 2.72 and -2.36 for the stable one (9f). Both, in the VLWF and the LSWF, a similar asymmetrical behavior is observed for the lateral fluxes of MKE as previously noted in Figure 8, and with values of 0.1 and -0.1 for the unstable-VLWF (9a), -0.03 and 0.03 for the neutral-VLWF (9b), and 0.06 and -0.05 for the stable-VLWF(9c). For the unstable-LSWF case results 0.01 and -0.02 (9d), 0.09 and 0.07 for the neutral-LSWF (9e) and 0.59 and 0.56 for the stable one (9f). Finally, attention should be placed to the asymmetric contribution in MKE through the bottom and top lids of the VLWF case (S_5 and S_6 respectively). This is the mechanism providing the recovery of most of the MKE depleted within the CV by the wind turbine; with values of -0.04 and 0.12 for the unstable (9a), -0.03 and 0.11 for neutral (9b), and -0.004 and 0.022 for the stable (9c). For the LSWF the contribution of MKE flux through the bottom and top lids is not so determining in the recovery of MKE, and it can also behave as an outflux of MKE, such in the neutral and stable cases (9e-f), due to the vertical slanted shape of the wake, especially during the stable regime.

To inform of the time evolution of the corresponding MKE contribution through the different surfaces of the wind turbine box, Figure 10 represents the individualized volume terms, now averaged every ten minutes instead of 1h periods trough the entire diurnal cycle. It corresponds to the previous bar plot (see Figure 9) as a function of time and with the individualized contribution of each volume term. First, it is important to note, that the behavior of the different terms do not exhibit variation as a function of time for the represented periods (unstable and stable), illustrating that the 1h averaging used through this study represents well the two different stratification regimes. Further, results illustrate that continuously in time the corresponding contributions through surfaces S_1 and S_2 remain the largest. It is worth noting the differentiated behavior between the VLWF and the LSWF cases, while the first almost presents negligible variation through the diurnal cycle, a more pronounced switch can be measured for the LSWF during the noon transition (between 10am and 1pm) in the fluxes through S_1 and S_2. Also, for the VLWF it is noticeable the enhanced flux through S_5 in comparison to S_6, $S_6 \approx 5S_5$ during the entire stable period (see Figure 10b), reflecting the earlier observed fact that most of the wake recovery is produced as a result of the vertical transport of MKE. In contrast, for the LSWF it is the lateral flux through S_4 that contributes the largest in the MKE recovery given that the fluxes through S_1 and S_2 almost perfectly compensate each other. It is also relevant to note the differentiated behavior for both cases, the VLWF and the LSWF, between the unstable and stable stratification periods, with large lateral oscillations on the fluxes through surfaces S_3 and S_4 (see Figures 10c and 10f).

VI. SUMMARY AND CONCLUSIONS

In this work an analysis of the distribution of the mean kinetic energy around a single wind turbine (LSWF) and a characteristic wind turbine of a very large wind farm (VLWF) under different atmospheric stability conditions (unstable, neutral and stable) are carried out. To accomplish a fair comparison, a dynamically yawed control volume (Wind Turbine Box) is utilized.

Results illustrate important characteristic differences in the recovery of MKE between a VLWF and a LSWF under different atmospheric conditions. As previously shown in other studies, the harvested power by the wind turbines

changes throughout the diurnal cycle, with a stronger power output during day-time and a reduction during night-time for the VLWF (reduction of 42%). This is a result of the enhanced mixing induced by the thermal stratification during day-time, and the vertical shift of the LLJ during night-time. Contrary, for the LSWF the maximum harvested power is obtained during night-time since the LLJ directly impinges with the rotor disk with an increase of 15%. In relation to this and for the case of a VLWF, the recovery of MKE is strongly dominated by the turbulent flux of MKE (ϕ), which presents a decreasing intensity with changing ABL stratification (32%, and 63% decrease for the neutral and stable stratified cases with respect to the unstable case, correspondingly). In contrast, for the LSWF, the recovery of MKE is shown to be dependent on the turbulent flux of MKE, the pressure redistribution term and the advection, being this last one the most important contribution. During the day-time the MKE depleted by the wind turbine is recovered by a contribution of 83% and during night-time the advection terms has a contribution of practically 100%. And during the neutrally stratified case, again almost the totality of the MKE recovery happens through the advection.

The analysis allows to identify the geometrical redistribution of MKE around a characteristic wind turbine. While the MKE fluxes through the front and backward faces (S_1 and S_2) are correspondingly the largest source and sink of MKE, they correspondingly compensate each other. Hence, the actual MKE recovery happens trough the lateral (S_3 and S_4) and vertical (S_5 and S_6) faces of the wind turbine box. Results clearly illustrate that during the convective regime the fluxes through the vertical faces of the wind turbine box dominate, while during the stable stratification the fluxes through the lateral surfaces are most important.

Finally, results also illustrate the fact that during the unstable regime the turbulent mixing around the wind turbines is dominated by the background atmospheric stratification, given that both, the LSWF and the VLWF, present a similar vertical shear at the top-tip of the rotor disk (only an 8% difference). Contrary, during night time, the mixing is dominated by the actual wind turbines, fact that is demonstrated by a much larger difference between the LSWF and VLWF vertical shear stress at the top-tip of the rotor disk (90% difference).

ACKNOWLEDGMENTS

Calaf acknowledges the Mechanical Engineering Department at University of Utah for start-up funds. Cal thanks the National Science Foundation for their support (NSF-CBET-1034581). The authors would like to recognize the computational support provided by the Center for High Performance Computing (CHPC) at University of Utah.

[1] GWEC, "Global Wind Report," Tech. Rep. (2014).
[2] N. Kelley and H. Sutherland, "Damage estimates from long-term structural analysis of a wind turbine in a U.S. wind farm environment," 35th Aerospace Sciences Meeting and Exhibit , 1–10 (1997).
[3] C. Sim, S. Basu, and L. Manuel, "On space-time resolution of inflow representations for wind turbine loads analysis," Energies **5**, 2071–2092 (2012).
[4] M. J. Churchfield, S. Lee, J. Michalakes, and P. J. Moriarty, "A numerical study of the effects of atmospheric and wake turbulence on wind turbine dynamics," Journal of Turbulence **13**, 1–32 (2012).
[5] H. Lu and F. Porté-Agel, "On the Impact of Wind Farms on a Convective Atmospheric Boundary Layer," Boundary-Layer Meteorology **157**, 81–96 (2015).
[6] D. Yang, C. Meneveau, and L. Shen, "Large-eddy simulation of offshore wind farm," Physics of Fluids **26** (2014).
[7] C. VerHulst and C. Meneveau, "Large eddy simulation study of the kinetic energy entrainment by energetic turbulent flow structures in large wind farms," Physics of Fluids **26** (2014).
[8] M. Abkar and F. Porté-Agel, "The effect of free-atmosphere stratification on boundary-layer flow and power output from very large wind farms," Energies **6**, 2338–2361 (2013).
[9] M. Abkar and F. Porté-Agel, "Mean and turbulent kinetic energy budgets inside and above very large wind farms under conventionally-neutral condition," Renewable Energy **70**, 142–152 (2014).
[10] C. VerHulst and C. Meneveau, "Altering kinetic energy entrainment in large Eddy simulations of large wind farms using unconventional wind turbine actuator forcing," Energies **8**, 370–386 (2015).
[11] M. Calaf, C. Meneveau, and J. Meyers, "Large eddy simulation study of fully developed wind-turbine array boundary layers," Physics of Fluids **22, 015110** (2010).
[12] R. B. Cal, J. Lebrón, L. Castillo, H. S. Kang, and C. Meneveau, "Experimental study of the horizontally averaged flow structure in a model wind-turbine array boundary layer," Journal of Renewable and Sustainable Energy **2** (2010).
[13] M. Calaf, M. B. Parlange, and C. Meneveau, "Large eddy simulation study of scalar transport in fully developed wind-turbine array boundary layers," Physics of Fluids **23** (2011).
[14] H. Lu and F. Porté-agel, "Large-eddy simulation of a very large wind farm in a stable atmospheric boundary layer," Physics of Fluids **23**, 065101 (2011).

[15] F. Porté-Agel, H. Lu, and Y. Wu, "Interaction between Large Wind Farms and the Atmospheric Boundary Layer," in *23rd International Congress of Theoretical and Applied Mechanics*, Vol. 10 (Elsevier B.V., 2014) pp. 307–318.
[16] B. Witha, G. Steinfeld, M. Dörenkämper, and D. Heinemann, "Large-eddy simulation of multiple wakes in offshore wind farms," Journal of Physics: Conference Series **555**, 012108 (2014).
[17] M. Dörenkämper, B. Witha, G. Steinfeld, D. Heinemann, and M. Kühn, "The impact of stable atmospheric boundary layers on wind-turbine wakes within offshore wind farms," Journal of Wind Engineering and Industrial Aerodynamics **144**, 146–153 (2015).
[18] G. S. Poulos, W. Blumen, D. C. Fritts, J. K. Lundquist, J. Sun, S. P. Burns, C. Nappo, R. Banta, R. Newsom, J. Cuxart, E. Terradellas, B. Balsley, and M. Jensen, "CASES-99: A comprehensive investigation of the stable nocturnal boundary layer," Bulletin of the American Meteorological Society **83**, 555–581 (2002).
[19] V. Kumar, G. Svensson, a. a. M. Holtslag, C. Meneveau, and M. B. Parlange, "Impact of surface flux formulations and geostrophic forcing on large-eddy simulations of diurnal atmospheric boundary layer flow," Journal of Applied Meteorology and Climatology **49**, 1496–1516 (2009).
[20] V. Kumar, J. Kleissl, C. Meneveau, and M. B. Parlange, "Large-eddy simulation of a diurnal cycle of the atmospheric boundary layer: Atmospheric stability and scaling issues," Water Resources Research **42**, 1–18 (2006).
[21] G. Svensson, a. a. M. Holtslag, V. Kumar, T. Mauritsen, G. J. Steeneveld, W. M. Angevine, E. Bazile, a. Beljaars, E. I. F. de Bruijn, a. Cheng, L. Conangla, J. Cuxart, M. Ek, M. J. Falk, F. Freedman, H. Kitagawa, V. E. Larson, a. Lock, J. Mailhot, V. Masson, S. Park, J. Pleim, S. Söderberg, W. Weng, and M. Zampieri, "Evaluation of the diurnal cycle in the Atmospheric Boundary Layer over land as Represented by a Variety of Single-Column models: The second GABLS Experiment," Boundary-Layer Meteorology **140**, 177–206 (2011).
[22] S. Basu, J. F. Vinuesa, and A. Swift, "Dynamic LES modeling of a diurnal cycle," Journal of Applied Meteorology and Climatology **47**, 1156–1174 (2007).
[23] V. Sharma, M. B. Parlange, and M. Calaf, "Perturbations to the spatial and temporal characteristics of the diurnally-varying atmospheric boundary layer due to an extensive wind farm," Boundary-Layer Meteorology , 128 (2016).
[24] G. Cortina, V. Sharma, and M. Calaf, "Investigation of the incoming wind vector for improved wind turbine yaw-adjustment under different atmospheric and wind farm conditions," Renewable Energy **101**, pp.376–386 (2017).
[25] A. C. Fitch, J. K. Lundquist, and J. B. Olson, "Mesoscale Influences of Wind Farms throughout a Diurnal Cycle," Monthly Weather Review **141**, 2173–2198 (2013).
[26] V. Sharma, M. Calaf, M. Lehning, and M. B. Parlange, "Time-adaptive wind turbine model for an les framework," Wind Energy **19**, 939–952 (2016).
[27] M. Abkar, A. Sharifi, and F. Port-Agel, "Wake flow in a wind farm during a diurnal cycle," Journal of Turbulence **17**, 420–441 (2016).

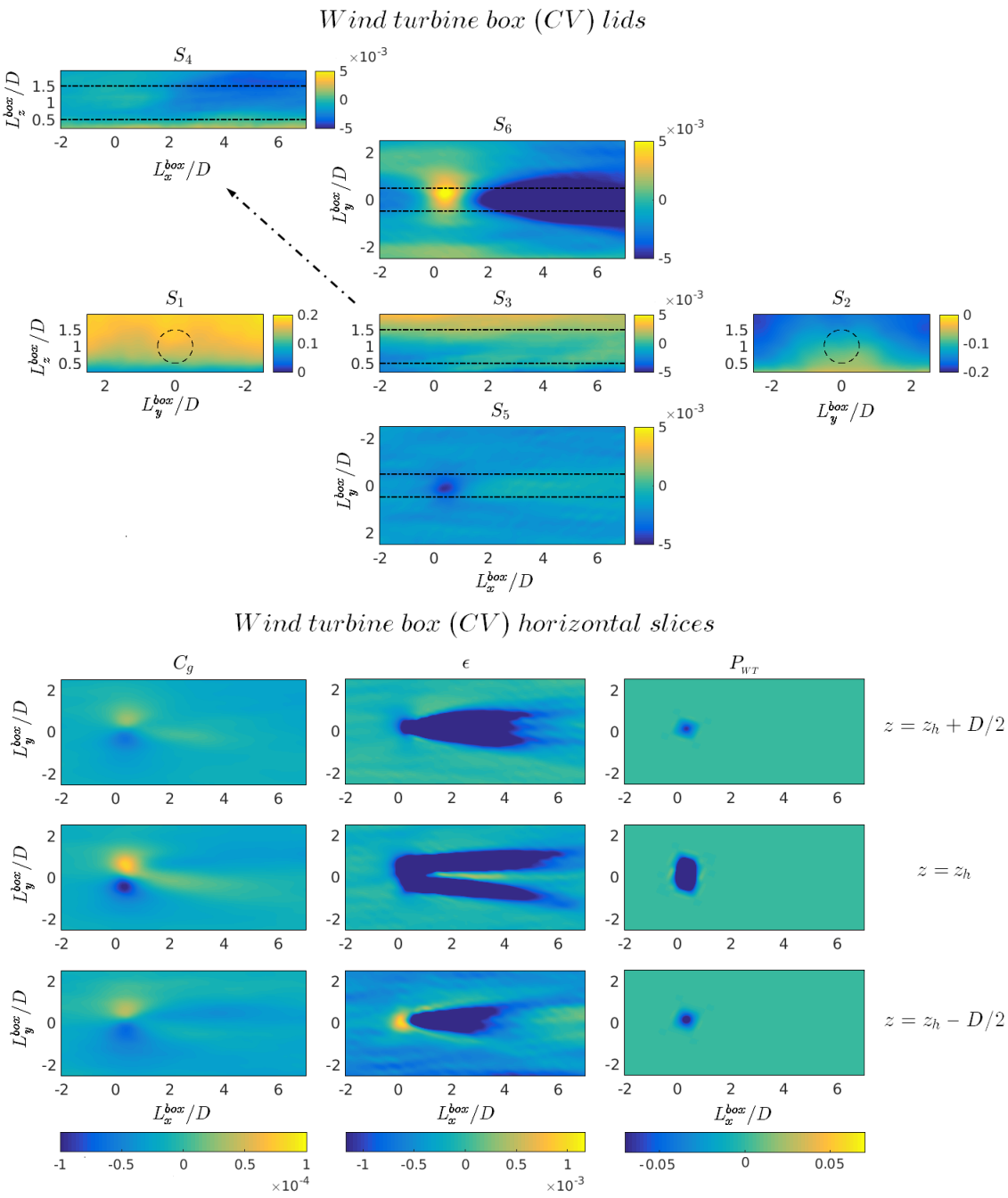

FIG. 7. Top subplots: representation of the contribution of the surface MKE terms (sum of the advection (A), turbulent flux (ϕ) and pressure term (P)) through the control surfaces at the different lids of the wind turbine box. Front (S_1) and back (S_2), right (S_3) and left (S_4), bottom (S_5) and top (S_6). Bottom subplots: horizontal slices at different heights ($z_h - D/2$, z_h and $z_h + D/2$) for the volume terms (C_g, ϵ, P_{WT}) contributing to the MKE budget normalized by the geostrophic velocity and the wind turbine diameter (D/U_G^3). The top and bottom subplots are representative of one-hour averaged data for the LSWF case during the unstable regime.

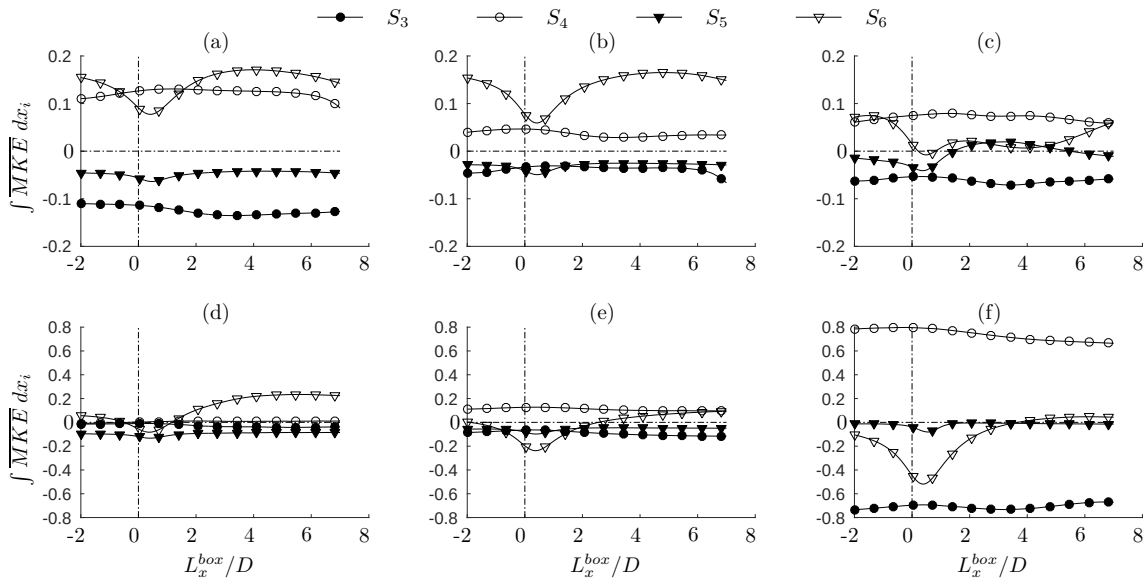

FIG. 8. Streamwise profiles of the wind turbine box, vertically integrated flux terms through the bottom (S_5) and top (S_6) lids and streamwise profiles of the wind turbine box horizontally integrated flux terms through the right (S_3) and left (S_4) surfaces. The flux terms are normalized by the cube of the geostrophic wind, the diameter of the wind turbine, and the length of the wind turbine box over which the integral is computed $D/(U_G^3 L_i^{box})$ where $i = 1, 3$. Subplots (a)-(c) represent the VLWF case, and (d)-(e) the LSWF case for the unstable, neutral and stable stratification, correspondingly. The vertical dashed line denotes the location of the wind turbine rotor.

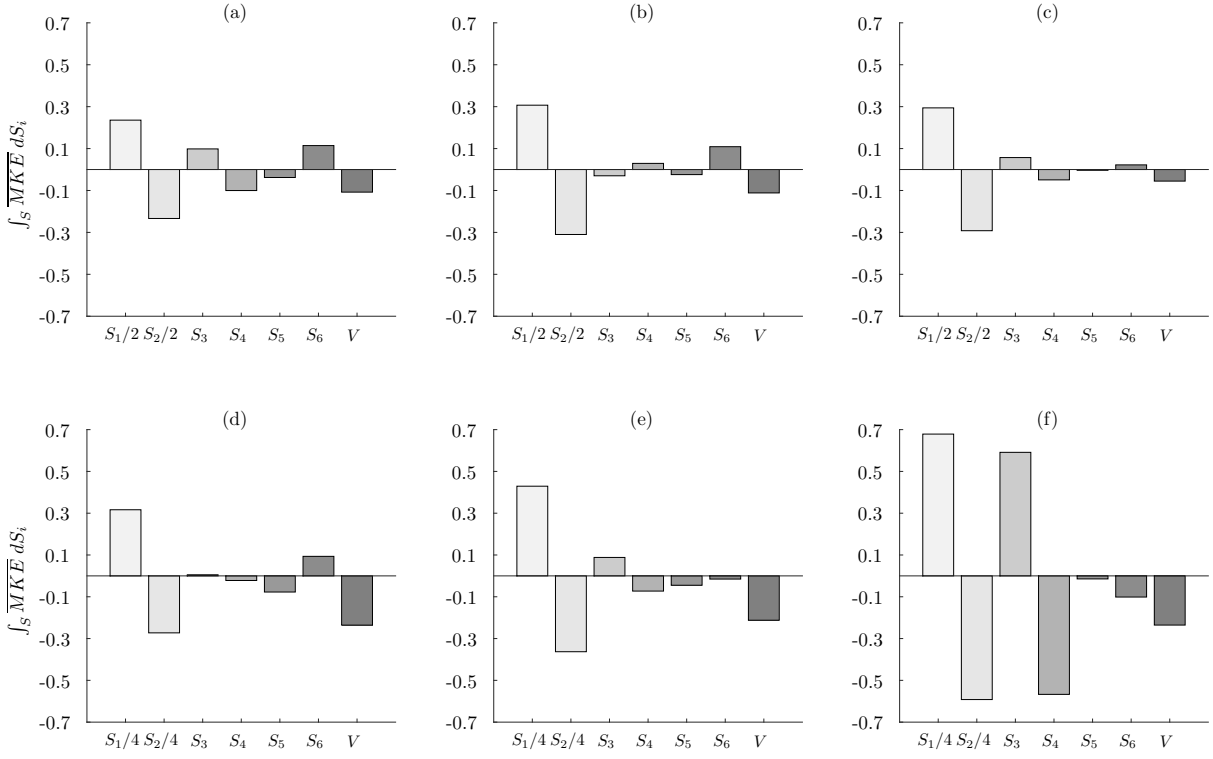

FIG. 9. Bar representation of the surface integral for the MKE flux through the distinct surfaces and volume terms. Each bar indicates the corresponding contribution of MKE through each face of the wind turbine box (S_1, S_2, S_3, S_4, S_5, S_6) and V representing the sum of the volume terms within the control volume. The flux terms are normalized by the geostrophic wind and the diameter of the wind turbine, resulting $(1/(U_G^3 D^2))$. Subplots (a), (b) and (c) depict the VLWF case for unstable, neutral and stable stratification, respectively. Subplots (d), (e) and (f) depict the LSWF case for the unstable, neutral and stable stratification, respectively. Notice that for the VLWF subplots, terms S_1 and S_2 are divided by 2 and for the LSWF subplots, the same terms are divided by 4 in order to be able to visualize the magnitude of the rest of the terms.

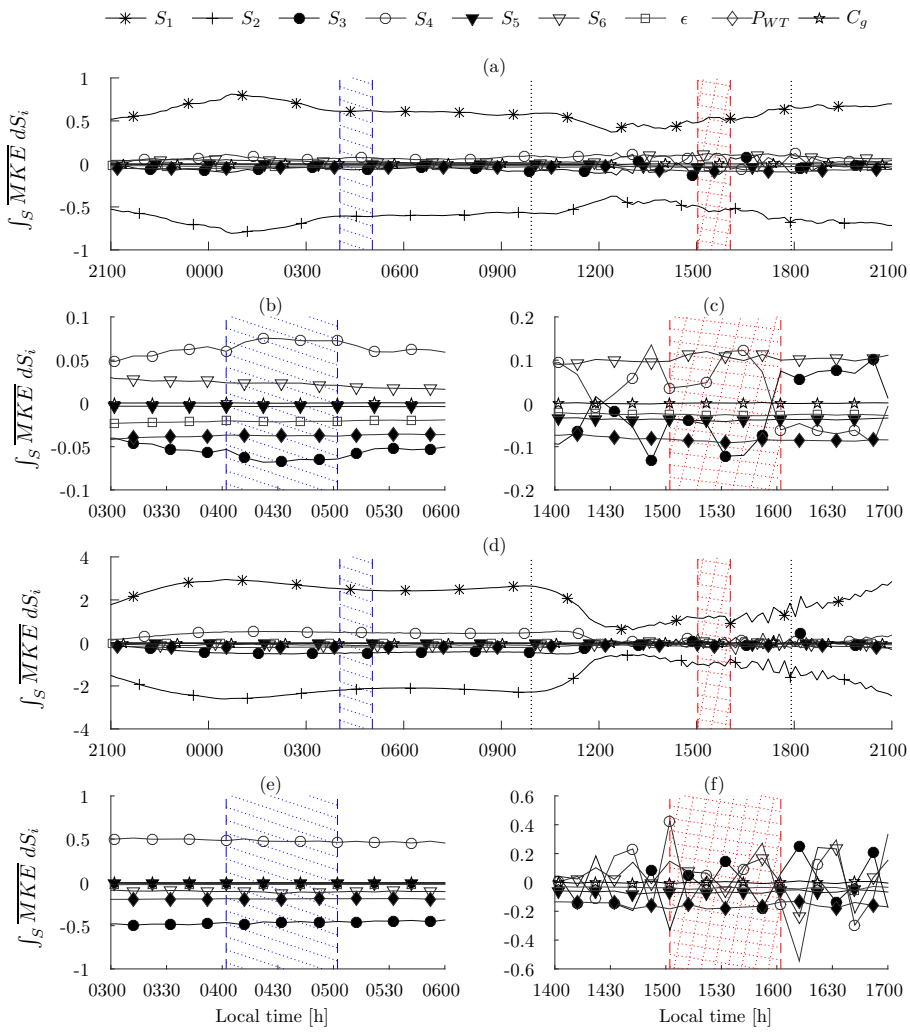

FIG. 10. Time-line representation of the 10minutes average surface integral for the MKE flux through the distinct surfaces $(S_1, S_2, S_3, S_4, S_5, S_6)$ and volume terms (ϵ, P_{WT} and C_g) for the wind turbine box. The flux terms are normalized by the geostrophic wind and the diameter of the wind turbine, resulting $(1/(U_G^3 D^2))$. Subplots (a), (b) and (c) depict the VLWF case and subplots (d), (e) and (f) depict the LSWF case during the diurnal cycle. Notice that subplot (b) and (c) are detail views of the stable and unstable regimes for the VLWF case, respectively. Subplots (e) and (f) are detail views of the stable and unstable regimes for the LSWF case, respectively.